Impact Resistance of a Free Sintering Low Alloy Steel Produced by Powder Bed Fusion Using a Laser Beam

Thomas F. Murphy, FAPMI, Christopher T. Schade, FAPMI, & Kerri M. Horvay
Hoeganaes Corporation
Cinnaminson, NJ 08077

ABSTRACT

Dual phase (DP) steels are utilized by designers in the automotive industry to take advantage of their ability to absorb high amounts of energy during crash events, thus improving driver and passenger safety. The locations in the vehicle chassis that benefit from their use are usually determined by the amount of energy that needs to be absorbed during an impact. With these energy-absorbing performance requirements in mind, a DP steel named free-sintering low-alloy (FSLA) was designed for use with metal binder jet printing (BJT) and implemented in both BJT and laser powder bed fusion (PBF-LB) to expand the use of additive manufacturing (AM) into these applications. The versatility of this DP alloy was demonstrated in previous papers [1-5], where multiple heat treatments were designed to provide the microstructure control needed to meet the wide range of mechanical properties of the wrought DP low alloy steels. It was shown that the proportions of the transformation products could be altered from nearly all ferrite to that consisting of high percentages of bainite and/or martensite with a minor amount of ferrite. In this paper, the impact energy of a variant of the original FSLA, FSLA Modified (FSLA Mod) is examined as a function of the microstructure developed through several heat treatments. The study focuses on the changes in the microstructure and the resulting fracture surfaces as they relate to their respective impact energies. This information can be used to design the proper heat treatment needed to produce the correct microstructure to satisfy the mechanical property needs for multiple applications.

INTRODUCTION

DP steels are a versatile class of Advanced High Strength Steels (AHSS) capable of possessing a wide range of mechanical properties by customization of their microstructures through heat treatment. The dual phase microstructures are produced by intercritically annealing these low-carbon steels in the two-phase, $\alpha + \gamma$ (ferrite + austenite), region of the phase diagram and cooling at a predetermined rate. The

microstructure resulting from this heat-treating process is a mixture of soft, ductile ferrite grains and regions of hard, strong martensite and/or bainite. The amount and type of each transformation product is determined by the intercritical annealing temperature and cooling rate, where the high temperature ferrite formed during annealing is stable at room temperature and the austenite transforms upon cooling. The annealing temperature determines the proportions and compositions of the ferrite and austenite at the elevated temperature, including the amount of carbon contained in the austenite.

The original FSLA was developed for use in AM with BJT, which is a solid-state process where the part is printed, then sintered to achieve densification and develop the mechanical and physical properties. With densification controlled by the sintering process, changes from the commercially available DP compositions were required because the more traditional DP alloys relied on Mn, an austenite stabilizer, for the bulk of the alloying. These more traditional alloys are austenitic, face-centered cubic (FCC), at sintering temperature and lack sufficient diffusion to create a highly densified part after sintering. With the desire to increase densification through sintering, the more typical DP composition was modified by nearly eliminating the austenite stabilizing Mn and increasing the use of ferrite stabilizers, Cr, Si, and Mo as the principal alloying elements. Figure 1 shows estimated ThermoCalc diagrams for a conventional DP steel, DP600, and the original FSLA. Through the range of sintering temperatures proposed for use with this alloy and shown within the areas bordered by the red lines, the DP600 is FCC, austenite, at all temperatures. Conversely, the FSLA is a combination of FCC and body-centered cubic (BCC), ferrite, throughout this temperature range and intended carbon content. The high BCC percentage provides the increased diffusion and densification required for the printed part to be successful. [6-9]
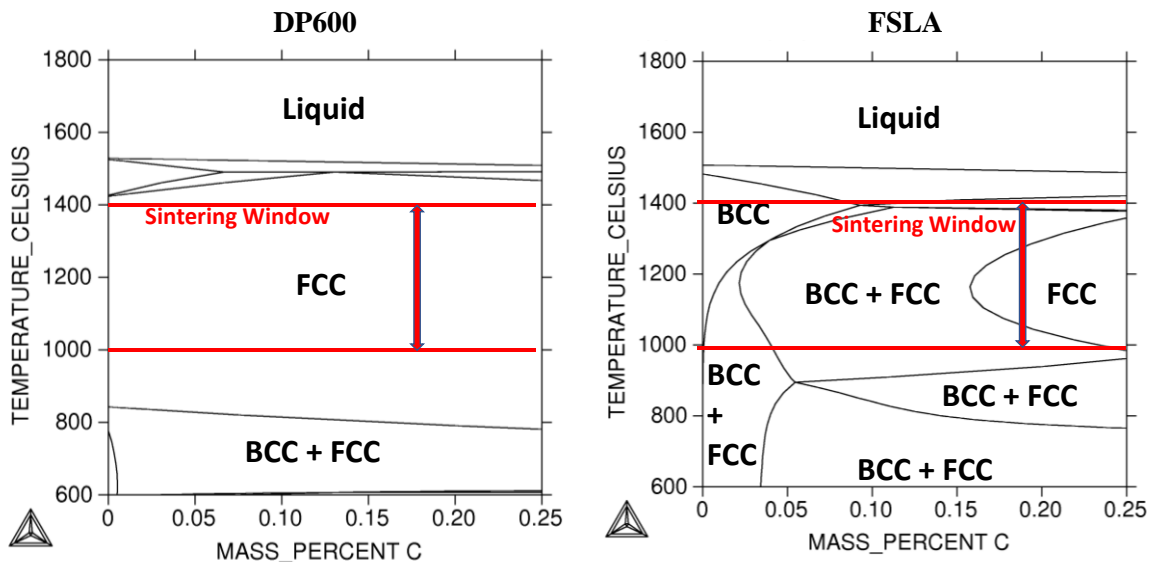

Figure 1. Estimated ThermoCalc phase diagrams for the conventional DP600 alloy and the original FSLA. The increased percentage of ferrite stabilizers, coupled with the low carbon levels, create the elevated temperature two-phase region in the FSLA.

The newly designed DP alloy, FSLA, was shown to be successful with the solid-state processing used for BJT. [1-2] However, since only one AM method was utilized in this testing, the inefficiencies of using approximately one-third of the full particle size distribution resulted in an increase to the powder cost. In an attempt to reduce these costs, tests were performed using other AM techniques, including PBF-LB, which relies on the formation of liquid from melting the powder by the laser for densification. [4] These

tests were also successful and consequently, the alloy was found to be applicable for both the solid and liquid-state processes. In both cases, the densified parts, one group from sintering and the other from solidification, were heat treated using similar intercritical annealing conditions and cooling rates. Since the same alloy was used in both types of processing, the heat-treating cycles produced similar, although not identical, microstructures and performance.

In the next phase of the DP steel development, the composition of the FSLA was modified by eliminating V and Nb, both strong carbide forming elements, to form the new FSLA Mod alloy. These two elements produce highly stable carbides, which could precipitate throughout the microstructure, leading to a loss in ductility (lower elongation) and possibly contribute to embrittlement. In this study where impact performance was of primary concern, embrittled microstructures and lower ductility are both detrimental to part performance.

EXPERIMENTAL PROCEDURES

The FSLA Mod powder used for these experiments was melted in an air atmosphere and gas atomized using nitrogen to create spherical particles like those shown in Figure 2. The chemical composition of the FSLA Mod is shown in Table I and compared with both the original FSLA that was the subject powder in the previous papers [1-5] and a commercially available dual phase steel, DP600. The DP600 was one of the more traditional AHSS alloys whose properties were a target for development of the DP steel suitable for AM processing. As mentioned in the Introduction, the difference between the two FSLA alloys was the elimination of two strong carbide forming elements, V and Nb, from the modified powder. Finally, the as-atomized powder was processed to the particle size distribution of 15-53 μm to meet the requirements of the PBF-LB process.
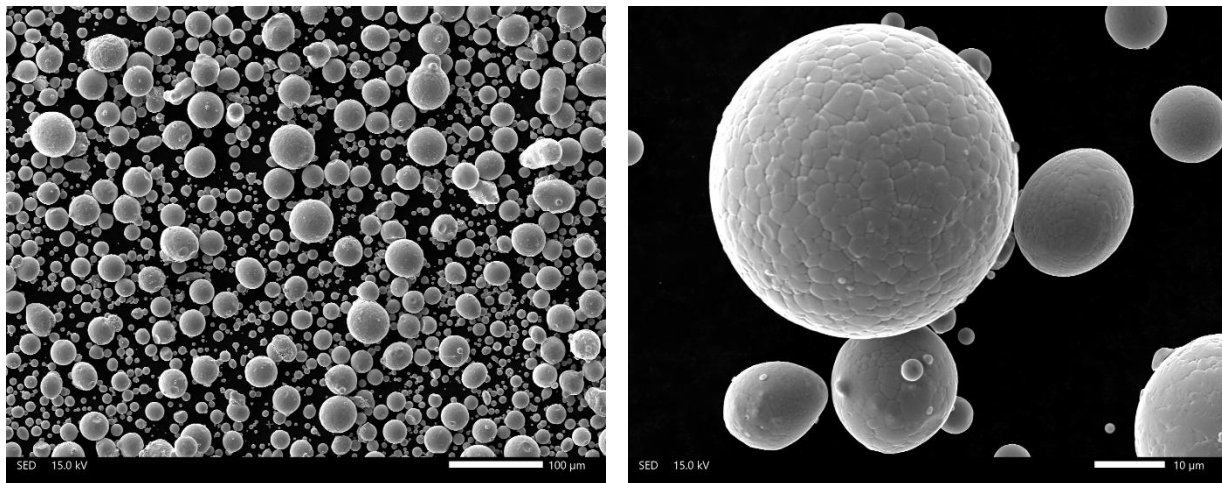

Figure 2. Appearance of the gas atomized powder at a lower magnification showing the size distribution of the powder mass and at a higher magnification emphasizing the surface detail of the particles.

The FSLA Mod chemical composition was formulated to enlarge the ferrite phase field at the BJT sintering temperatures, thereby increasing the amount of densification to the porous printed part since diffusion with BCC ferrite is far greater than that with FCC austenite. The increase in the amount of ferrite stabilizers, Cr, Mo, and Si, coupled with the decrease in the primary alloying element used in commercially available DP steels, Mn, an austenite stabilizer, resulted in an expansion of the high temperature BCC + FCC phase field shown in Figure 1 and provided the opportunity for greater

densification during sintering. In addition, these ferrite stabilizing elements increase the hardenability of the alloy. Consequently, microstructures containing the stronger and harder transformation products, martensite and/or bainite, can be attained using slower cooling rates from the heat-treating temperatures.

While the original FSLA composition was developed for BJT, a solid-state process, efforts were made to expand use of the alloy into other AM techniques to help offset some of the cost inefficiencies from using only a small portion of the particle size distribution with a single technique. Experiments were performed using another solid-state technique, metal injection molding (MIM), and two liquid phase methods, PBF-LB and directed energy deposition (DED) with favorable results from all tests. [5] These successes demonstrated particles with diameters as large as 100 μm could be used in other AM methods, thus lowering the powder costs.

Table I.
Chemical Compositions (wt.%)
(DP600 values are maximums) [10]

	C	S	Mn	Cr	Mo	Si	V	Nb	Cu
FSLA Mod	0.14	0.007	0.02	1.81	1.53	1.42	0.01	0.01	0.04
FSLA Original	0.14	0.007	0.20	1.60	1.45	1.64	0.18	0.18	0.03
DP600*	0.15	0.01	2.5	1.4 Max Total		0.8	Not Added Intentionally		0.2

* The value following the DP designation refers to the ultimate tensile strength of the alloy in MPa.

An EOS M290 AM machine, with build dimensions of 250 mm x 250 mm x 325 mm, was used to make the PBF-LB Charpy impact bars by melting the FSLA Mod powder layer by layer with a Yb fiber laser (400W) inside an argon filled chamber. A constant powder layer thickness was used, with the laser power, scanning speed, and hatch distance varied to find the optimal energy density for the FSLA Mod powder. Once these variables were optimized, a set of standard settings was deveoped and used to build the impact bars.

The bars were oriented in the vertical direction, with the longest dimension perpendicular to the build plate. The as-built bars were made 1 mm oversize to permit machining of the rough, as-built surfaces. The bars were cut from the build plate, then the surfaces and notch were machined to meet both the dimensional and roughness requriements of ASTM Standard Test Method E23. [11] Figure 3 provides the dimensions of the bars and notch as required by the standard. [12]
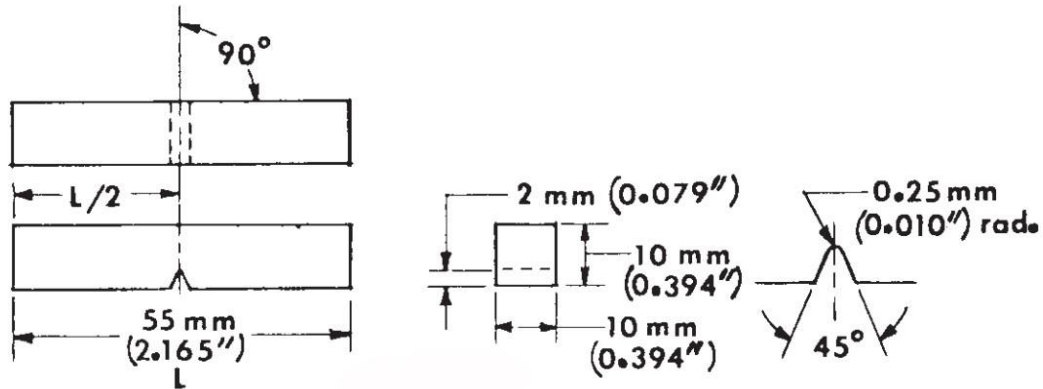
Figure 3. Dimensions of the Charpy V-notch impact bars prior to testing.
In this instance, the drawing from a superseded version of ASTM E23 was used because, in addition to specifying dimensions in SI units, the inch-pound units are included for information purposes only.

After machining, bars were tested in both the as-built and heat treated conditions. The as-built microstructure was the starting condition for all heat treatments, where the temperatures chosen for the subsequent thermal processing cycles were selected from the CALPHAD-generated equilibrium graph in Figure 4. The original FSLA composition was used as the basis for this graph and, although the composition of the FSLA Mod was altered slightly, the curves can be used as a good approximation of the temperature-microstructure relationships for the modified composition. Two heating temperatures were used before cooling. They were 800 °C (≈1475 °F) and 1200 °C (≈2200 °F). As seen in Figure 4, the microstructure at 800 °C is primarily ferrite and at 1200 °C, it is nearly all austenite. In addition, two cooling rates were utilized to vary the final transformed microstructure. Specifically, the four thermal cycles used for modifying the microstructure of the as-built samples are shown in Table II.
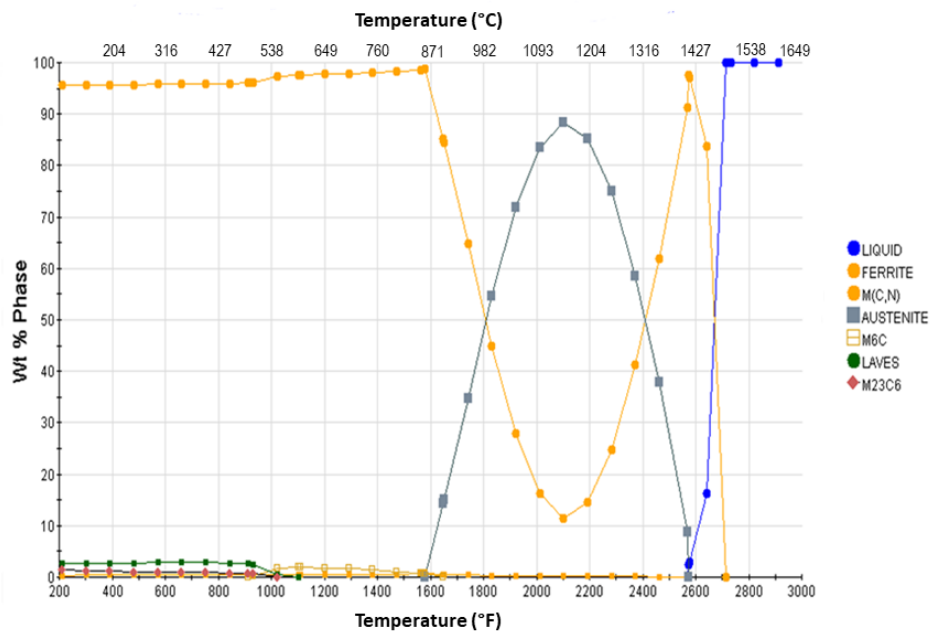

Figure 4. CALPHAD generated diagram showing the temperature-phase relationships of the FSLA.

Table II.
Thermal Histories of the Five Impact Bar Groups

Group No.	Heating	Cooling	Intent
1	As Built	Variable	
2	800 °C for 30 min.	50 Hz Gas Quench	High temperature temper with no formation of austenite
3	1200 °C for 1 hr. reduced to 800 °C for 2 hrs.	50 Hz Gas Quench	Austenitize, then reduce temperature to form ferrite
4	1200 °C for 5 hr.	50 Hz Gas Quench	Austenitize for longer time, then slower cool to form bainite + martensite
5	1200 °C for 1 hr.	Water Quench	Austenitize for shorter time then, faster cool to form bainite + martensite

The as-built and heat treated Charpy impact bars were tested using a standard pendulum impact tester. An example of the device is shown in Figure 5a. [13] In operation, the pendulum containing the striking hammer is raised to an initial height, which is the predetermined amount of potential energy used to strike the bar when the pendulum is released. The bar to be tested is placed against an anvil in the path of the pendulum swing with the notch facing away from the hammer (striker), as shown in Figure 5b. [14] When released, the pendulum swings, strikes the bar breaking it, and continues the swing to a height lower than the starting height. The difference between the starting and finishing heights is shown on the scale at the top of the tester. This is the amount of energy absorbed by the bar, e.g., the impact energy.
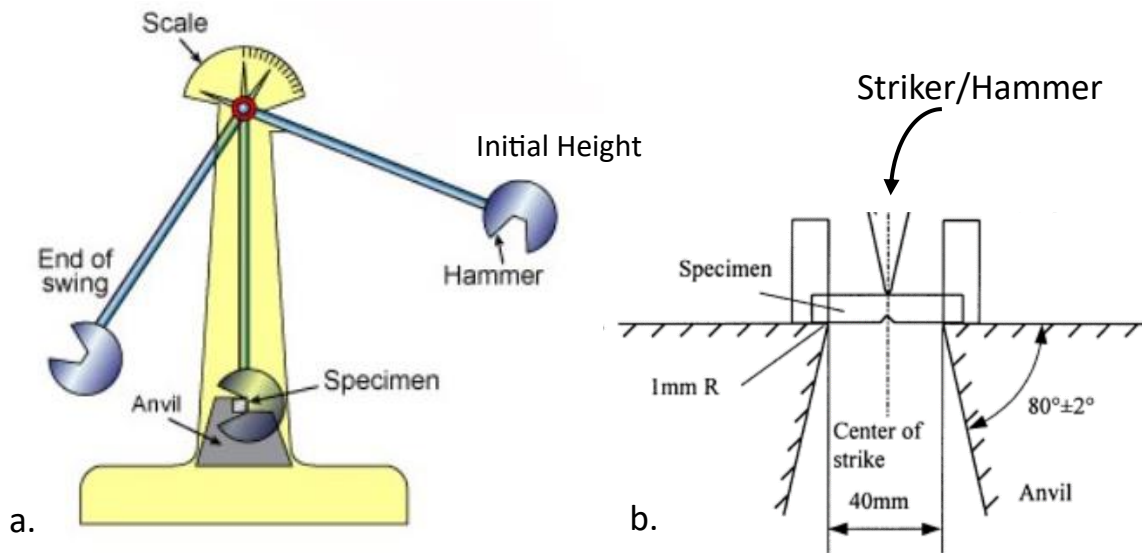

Figure 5. Drawings of (a.) the impact tester with locations of the pendulum containing the hammer, Charpy specimen, and scale indicating the impact strength and (b.) an overhead view of the anvil with dimensions and the locations of the Charpy bar and striker.

Metallographic testing was performed on cross-sections removed from the tested samples. These were prepared for examination using standard metallographic sectioning, mounting, grinding, and polishing techniques. The prepared samples were etched using Vilella's Reagent (5 ml hydrochloric acid [HCl] + 1 g picric acid [$C_6H_3N_3O_7$] + 95 ml ethyl alcohol [C_2H_5OH]), rinsed under running warm water, then

alcohol, and finally dried using a stream of compressed gas. Both light optical microscopy (LOM) and scanning electron microscopy (SEM) were used for the comparative examinations, which included general microstructure, feature size and location, grain size, local chemical composition of selected features, and others. In addition, quantitative volume fraction estimates of the transformation products were made on samples containing the dual phase microstructure using the Systematic Manual Point Count test method, ASTM E562. [15] Determination of grain size on the two primarily ferritic samples conformed to ASTM Standard Test Method E112. [16] Microindentation hardness was also measured on phases in the two samples that were primarily ferritic as described in ASTM Standard Test Method E384 [17] using a Matsuzawa Hardness Tester. SEM analysis was performed on the etched samples using a JEOL JSM-IT700HR microscope. Secondary electron images (SEI) were used for surface and feature analysis and imaging with backscattered electrons (BEI) revealed local atomic number compositional differences. Low magnification photomicrographs of fracture surfaces were captured using the vertical montage, Z-stack, imaging capability of a Leica M205A stereomicroscope.

RESULTS & DISCUSSION

The versatility of the original FSLA was demonstrated in the previously referenced papers [1,2] through the ability to customize the microstructure using intercritical annealing, thereby creating microstructures that would match application requirements. Similar heat treatment cycles were used to control the proportions of the transformation products in the FSLA Mod, since the only significant difference between the two alloys was the virtual elimination of V and Nb from the chemical composition.

Where the focus of the previous studies was to match the AM tensile properties of the FSLA to the commercially available DP steels by altering the balance of the transformation products, the purpose of the current study was to determine the impact toughness of the FSLA Mod through similar modifications of the microstructure, again through heat treatment.

Impact bars were heat treated using the four annealing/cooling cycles shown in Table II. Those used for groups 2 and 3 were designed to provide a microstructure that was primarily ferrite, while groups 4 and 5 were intended to be bainite and ferrite or possibly a combination of martensite, bainite, and ferrite. The five groups were impact tested using the method described in the Experimental Procedure section, with the heat-treating cycles and corresponding impact results shown in Table III.

Table III.
Impact Test Results

Group	1	2	3	4	5
Processing Conditions	As Built	800 °C for 30 min Gas Quench	1200 °C 1 hr – 800 °C 2 hr Gas Quench	1200 °C 5 hr Gas Quench	1200 °C 1 hr. Water Quench
Impact Energy (J)	46.2	179.7	6.8	24.7	54.6

Microstructure

Figure 6 shows the microstructure in an as-built (Group 1) sample and what was the starting microstructure for the four heat treatment procedures. In this condition, a fine-scale bainite was produced by transformation of the austenite during either solidification from laser melting or the repeated heating and cooling from the layer-by-layer building of the part. In addition to transforming the austenite to bainite during cooling, the bainitic carbides may have undergone slight self-tempering from the building process and the heating/cooling cycles.
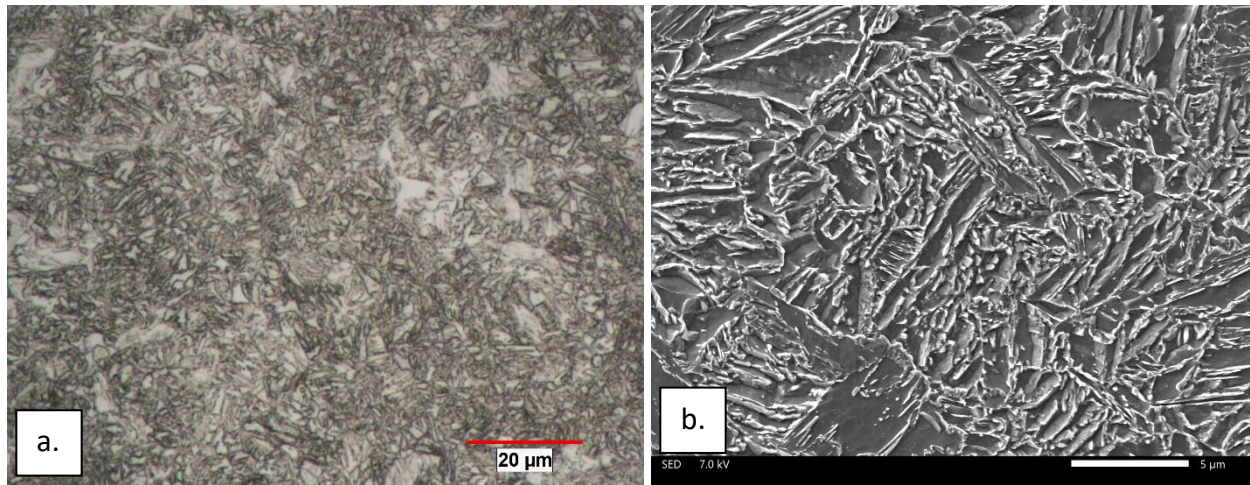
Etched using Vilella's Reagent

Figure 6. As-built photomicrographs, (a.) acquired using LOM, scale marker is 20 μm and (b.) SEM (SEI) image with scale marker 5 μm. The fine-scale microstructure is partially resolved using LOM (a.), while the organization of the carbide precipitates in the bainitic ferrite is clear in the (b.) image.

As mentioned earlier, the thermal processing cycles for Groups 2 and 3 were used to create primarily ferritic microstructures and hopefully, an increase in impact energy. The microstructures from these two groups were of particular interest because of the wide disparity in their impact energies. In the Group 2 heat treatment, the as-built bars were heated to 800 °C for 30 min, then gas quenched. This was essentially a high temperature temper, since the heating temperature was below the austenite transformation temperature, which would be closer to 860 °C. Figure 7 is representative of the microstructure in the Group 2 samples. It is a ferritic matrix with a distribution of fine, dot-like carbide precipitates. The carbides are nanometer-size features distributed throughout the microstructure, both in grain boundaries and in the grain interiors.

Images from the second ferrite heat treatment, Group 3, are displayed in Figure 8 and show significant microstructural differences compared with the Group 2 images. These samples display a substantial increase in grain size and elemental partitioning has occurred evidenced by areas of martensite mixed with bainite. The (a.) portions of Figures 7 and 8 were acquired at the same magnification to provide a direct comparison of the etched microstructures. In the Group 3 samples, the initial heat treating temperature was in the two-phase region, which caused a partitioning of the alloying elements, in addition to causing the large grain growth. It should also be recognized the carbide precipitates are located only in the ferrite phase and not in the higher hardness phase since the carbon is soluble in the austenite prior to transformation and not in the ferrite.
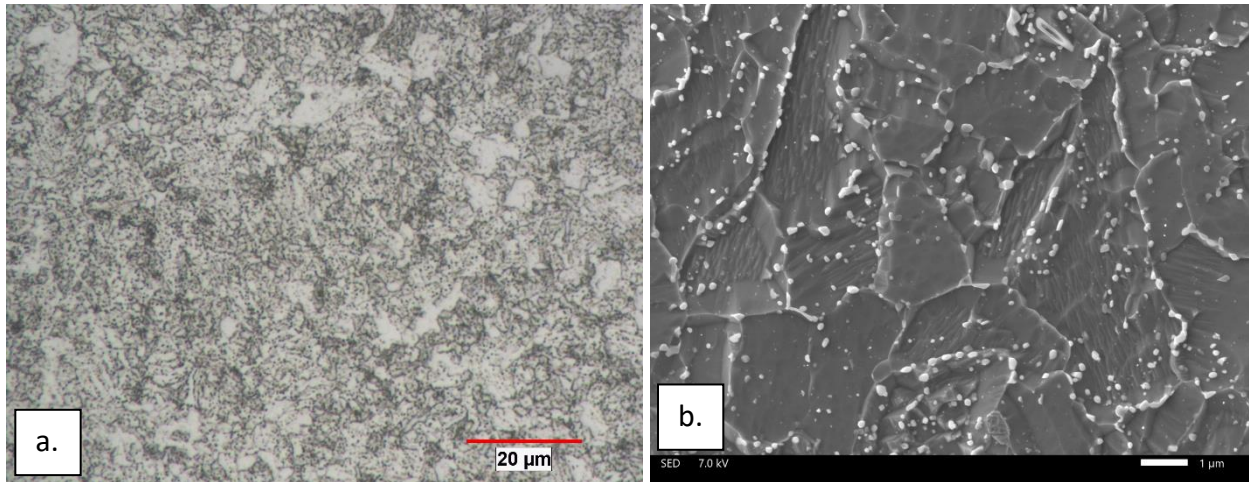
Figure 7. Photomicrographs from a Group 2 sample, with the (a.) image acquired using LOM, scale marker at 20 µm and the (b.) SEM (SEI) image with a 1 µm scale marker. The distribution of the fine precipitates is partially resolved using LOM (a.), while ferrite grain boundaries and the nanometer-size carbides, both at grain boundaries and interiors, are resolved in the (b.) image.
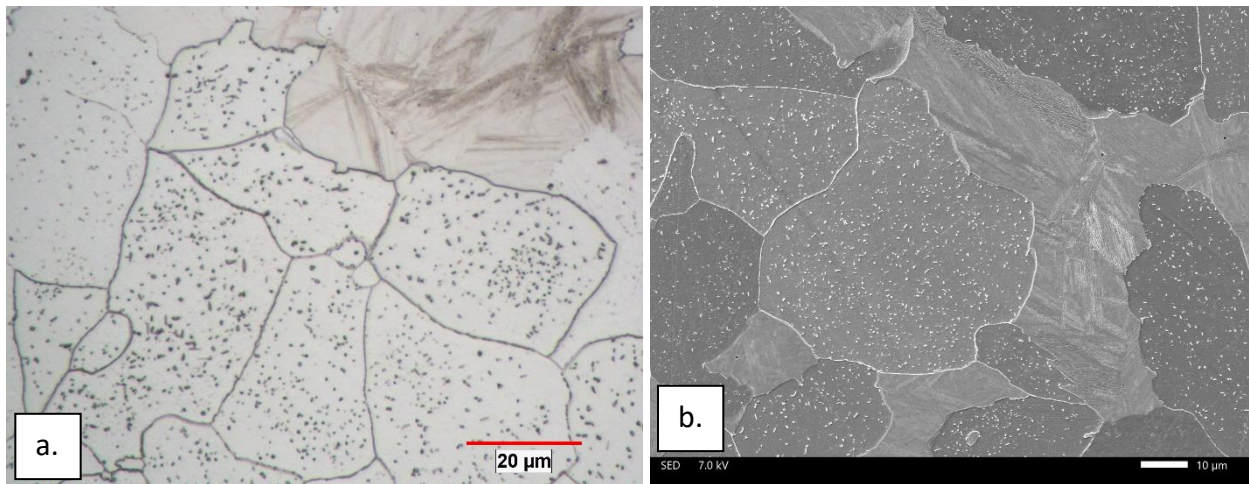
Figure 8. Photomicrographs from a Group 3 sample, with the (a.) image acquired using LOM, scale marker at 20 µm and (b.) the SEM (SEI) image with scale marker at 10 µm. The grain size is considerably larger compared with Fig. 7a and there is a portion of the cross-section that has transformed to bainite and martensite. Carbide precipitates are visible as the small dark dots in the (a.) image and as bright pinpoints in the (b.) image.

Further comparisons between Groups 2 and 3 were made by measuring the microindentation hardness (MIH) of the phases, estimating the phase proportions, estimating the grain size, and imaging using atomic number sensitive BEI to search for variations in chemical composition.

The volume percentage estimates and microindentation hardness measurements of the transformation products for these two groups are shown in Table IV. The Group 2 samples contained only ferrite, while those in Group 3 were a dual phase combination of ferrite with regions of bainite mixed with martensite

(≈20 vol.%). With the difference in heat treating conditions, the bars in Group 3 experienced alloy partitioning to form the high temperature ferrite-austenite microstructure, which resulted in the dual phase microstructure after cooling. In comparison, the bars in Group 2 experienced no or extremely limited partitioning and remained ferritic during the heat treatment. As a probable consequence, the ferrite in the Group 2 bars was harder compared with the ferrite in Group 3, most likely due to the presence of a higher percentage of alloying elements. Both groups exhibited the distribution of fine carbides throughout the ferrite.

Table IV.
Phase Percentage Estimates &
Microindentation Hardness Measurements

| | Group No. | Transformation Product | | |
		Ferrite	Bainite	Martensite
Phase Percentage (vol.%)	2	100	–	–
	3	79.4	20.6	
Microindentation Hardness (HV 0.1)	2	263	–	–
	3	186	522	646

The higher heat treating temperature experienced by the Group 3 samples also resulted in substantial grain growth compared with the Group 2 samples. Examining the LOM (a.) images acquired at the same magnification in Figures 7 and 8, the difference in grain size is obvious. Table V shows an estimate of the grain size in the two samples. Although the same alloy was used for all the experiments, this variation in grain size is likely responsible for large differences in both physical and mechanical properties.

Table V.
Ferrite Grain Size

Group No.	Average Intercept Distance (μm)	Grain Size (ASTM No.)
2	2.0	14.70
3	24.2	7.44

Another effect of the variation in ferrite heat treatment procedures can be seen in Figure 9, BEIs of the Groups 2 and 3 cross-sections. The atomic number sensitivity of BEI reveals differences in local chemical composition with features composed of higher atomic number elements appearing brighter than the surrounding area. The two images show the carbide precipitates as small bright features, indicating the presence of heavier elements. The locations of these heavier element precipitates are different in the two images. In the Group 2 (a.) image, they are distributed as small, dot-like features throughout the microstructure, including within the grain interiors and at grain boundaries. In comparison, the (b.) image from Group 3 also contains the small precipitates in the grain interiors, however, carbide precipitates decorate large portions of grain boundaries, with several of the carbides indicated with white arrows. These will contribute to embrittlement of the microstructure. In addition to these brighter carbides, it is possible carbides composed of lighter elements are also precipitated in these regions, which would also contribute to the embrittled microstructure.
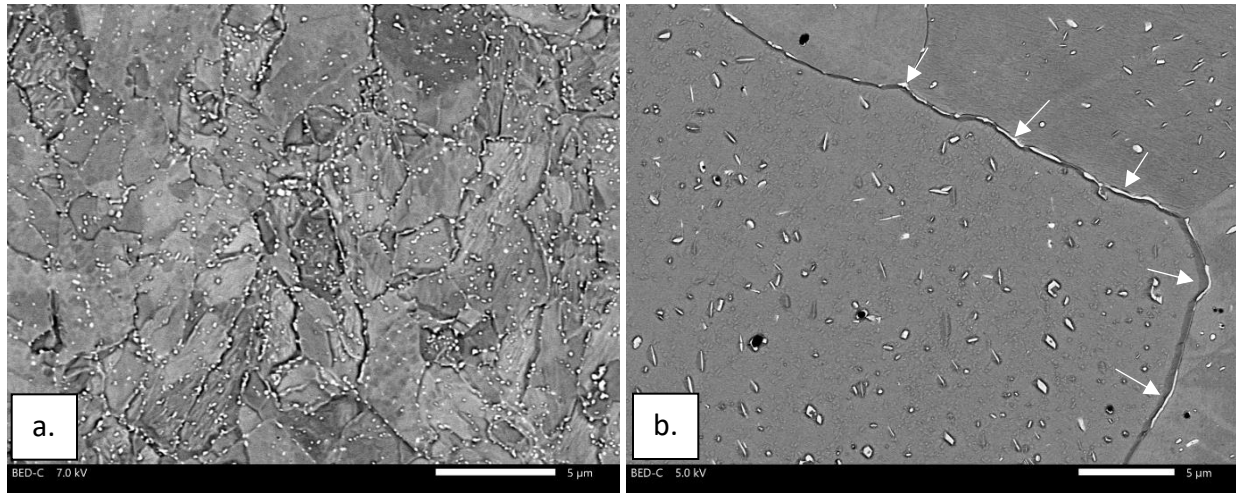
Etched using Vilella's Reagent

Figure 9. BEIs from Groups 2 and 3 showing the locations of carbides in the cross-sections. The scale markers for both images are 5 μm. In the (a.) image from Group 2, bright pin-point carbide precipitates are present throughout the cross-section. The Group 3 (b.) image shows bright carbide precipitates in both the grain interiors and as long, thin, bright features in the grain boundaries (see the white arrows).

To determine the composition of these nanometer size carbides, energy dispersive spectroscopy (EDS) was performed on individual precipitates in both samples. An example is included as Figure 10a, which shows a randomly selected carbide from a Group 2 sample marked with the red cross in the SEM/SEI photomicrograph. An EDS spectrum of this carbide is included as Figure 10b. The spectrum shows the carbide contained a significant amount of Mo, as indicated with the blue arrow at the Mo Lα energy location. Caution should be exercised when viewing this EDS spectrum because the feature size is likely smaller than the excitation volume from sample interaction with the electron beam. Consequently, the result of the analysis includes, not only the feature-of-interest, but probably a contribution from the surrounding sample volume.
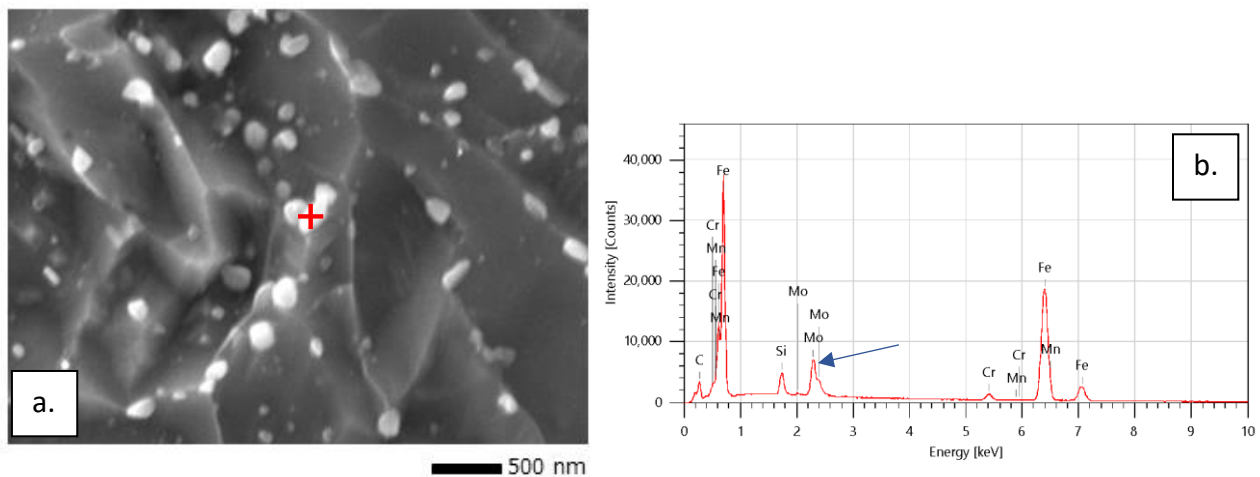

Figure 10. SEM/SEI location from a Group 2 sample etched using Vilella's Reagent. The (a.) portion shows the topographic surface created by chemical etching, including the small white carbide precipitates. The EDS spectrum, (b.), shows the elements present at the location in (a.) marked with the red cross as the peaks red line curve. The Mo Lα location is highlighted with the blue arrow.

Groups 4 and 5 were austenitized at 1200 °C, however for different times and their cooling rates were different. The bars heat treated in Group 4 were at temperature for approximately 5 hours and gas quenched in the heat treating furnace. In comparison, the bars from Group 5 were at temperature for 1 hour and rapidly cooled using a water quench. The microstructures from these two groups follow as Figures 11 and 12.

With bars from both groups undergoing heating in the primarily austenite phase field, the elevated temperature microstructure before cooling is nearly all austenite. However, the variation in hold time may have an effect on the homogeneity of the alloying elements and there could be variations in the local chemical composition. As Figures 11 and 12 show, both as-cooled microstructures are bainitic with the cooling rate causing the morphology of the carbide precipitates to be considerably different. Neither group has a true dual phase microstructure since the temperature from which the bars were cooled was in the nearly single phase, austenite region.

In viewing the two microstructures, Group 4 appears as a uniform distribution of fine bainitic carbides in a ferrite matrix. The packets are somewhat loosely defined, as is the grain structure. The longer hold time at the elevated temperature seems to have created a uniform distribution of alloying elements, as evidenced by the uniformity of the microstructure.
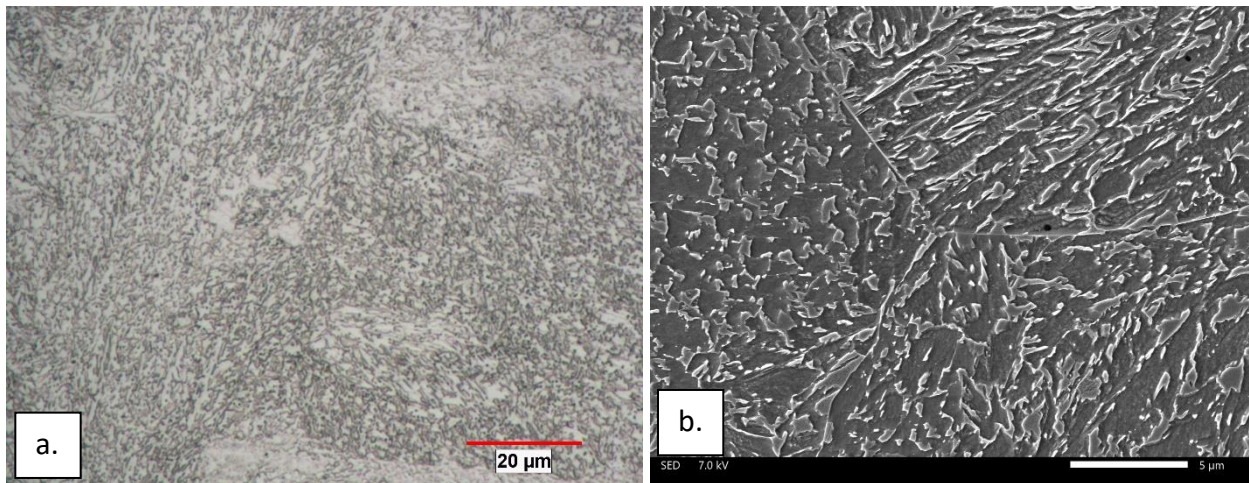
Etched using Vilella's Reagent

Figure 11. Photomicrographs from the bars in Group 4, with the (a.) image acquired using LOM, scale marker at 20 μm and (b.) the SEM (SEI) image with scale marker at 5 μm. Resolving the fine microstructure using LOM, (a.), is difficult, however the distribution of the bainitic carbides in the ferritic matrix is clear in the SEM/SEI (b.) image.

The microstructure of the Group 5 bars shows a clear but different bainitic transformation caused by the combination of the high temperature hold time and faster cooling rate. The bainitic packets are considerably better organized and the precipitated carbides in Figure 12b are longer and thinner compared with Figure 11b. In addition, the carbide distribution is somewhat different, with the ferrite more incorporated in the bainite packets rather than appearing as a matrix phase.
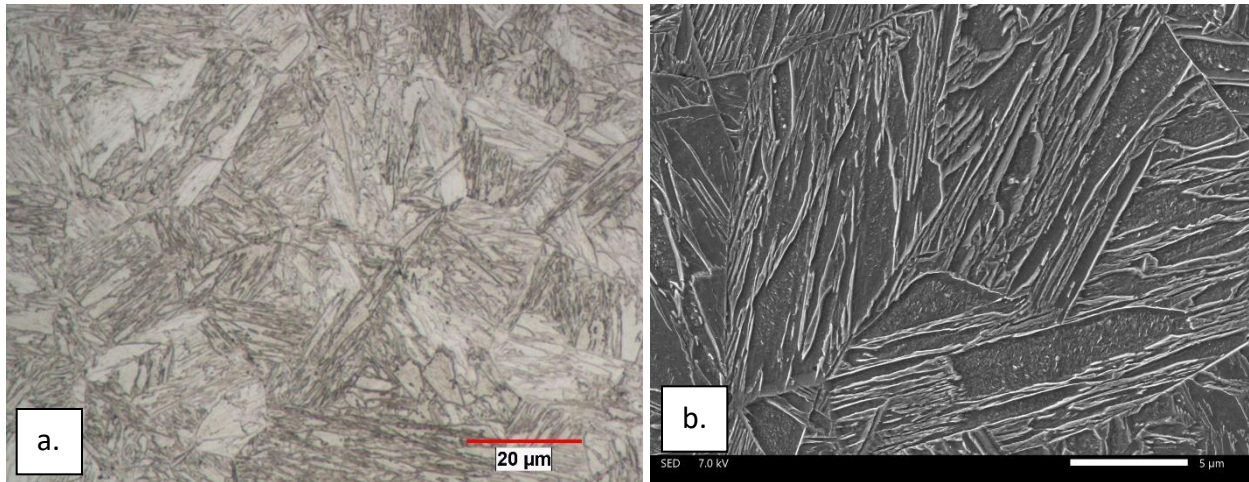
Etched using Vilella's Reagent

Figure 12. Photomicrographs from the bars in Group 5, with the (a.) image acquired using LOM, scale marker at 20 μm and (b.) the SEM (SEI) image with scale marker at 5 μm. The bainitic microstructure is more resolved in the (a.) LOM image compared with Figure 11a and the packets more organized.

Fracture Surface Analysis

The different heat treatments were employed to create variations in the microstructures and therefore, a range of impact strengths. With the strength differences, the appearance of fracture surfaces also varied. This is demonstrated on a macroscopic scale using photomicrographs from a stereo microscope in Figure 13. These show the entire fracture surface with the notch oriented at the top of each image. The images are annotated with the group number and the average impact strength from the bars in the group.
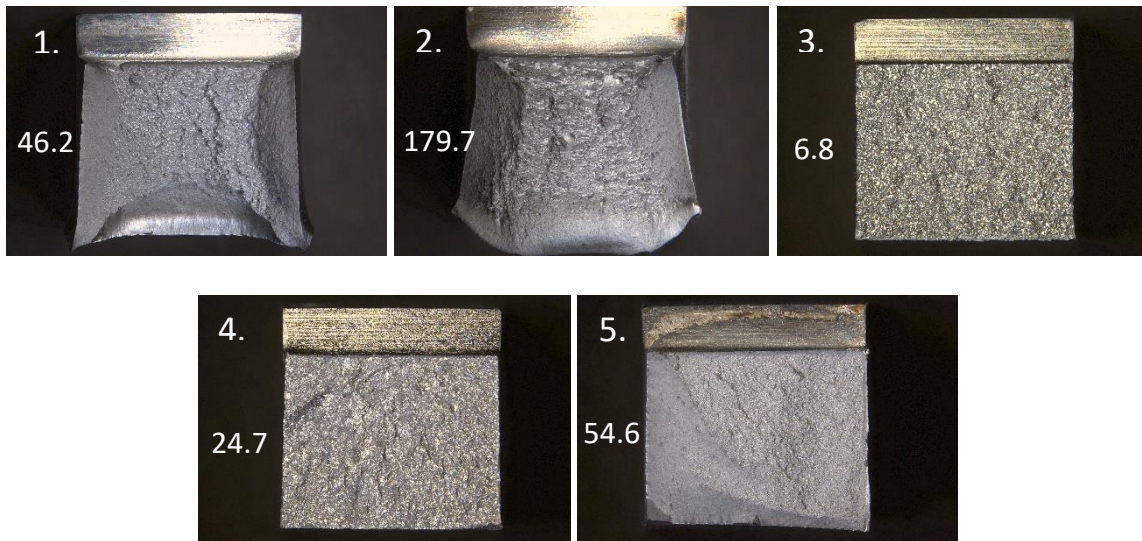
Figure 13. Images of a representative fracture surface from the five sample groups are shown for comparison. The white label numbers, 1 through 5, correspond to the group number from Table II and the second value is the average impact energy of the group.

The details contained on the fracture surface, both in macro and micro scale, describe the mechanism of fracture. The drawing in Figure 14 shows the locations of the different fracture regions. [12]   It is also

oriented the same as the macro-images in Figure 13, with the notch located at the top edge. When tested, the bar is impacted by the striker, which would be at the bottom of the image, causing failure to initiate just below the notch at the top. The fracture proceeds through the center of the cross-section, along the vertical edges forming shear lips if sufficient ductility is present, finally ending at the bottom edge. Each of these regions may display unique combinations of characteristics from the fracture due to the local microstructure and strength.
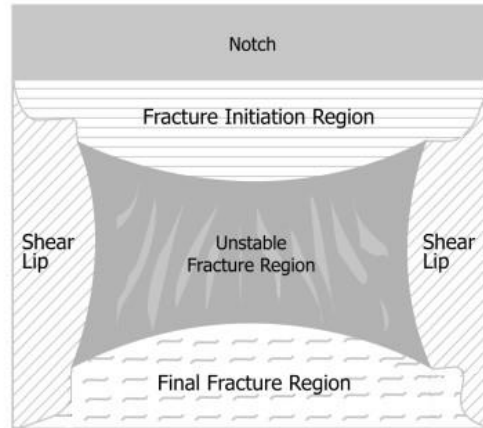
Figure 14. Schematic of the regions of fracture on a tested impact bar.

The photomicrographs in Figure 13 indicate bars from two groups, numbers 1 and 2, failed in the manner described in the schematic in Figure 14. The surfaces from the other groups display substantial amounts of brittle appearance, lacking the surface topography typical of more ductile materials.

SEM/SEIs are shown in Figure 15 to illustrate the regional differences in fracture characteristics on a single surface by moving across each row, and the differences in the same location between the five heat treated groups by moving up and down each column. The progression of fracture is from the top of each image, moving down, as indicated by the arrow at the right and all images are oriented with the notch at or toward the upper edge. The impact energy for each group is also included in the individual group labels to show the appearance of the fracture with the impact energy and to provide a comparison between groups.

Given the microstructural and impact energy differences between groups, it was expected the appearance of the fracture surfaces would be substantially different. In Group 1, the initiation and final fracture images show microvoid coalescence indicating ductility. In the center, the unstable fracture region is a combination of ductile dimpling and quasi-cleavage. In Group 2, all images indicate the fracture occurred by microvoid coalescence, although the size and shape of the dimples varied slightly in the center region, where there appears to be a slight directionality to some of the dimples in the unstable fracture region. In Group 3, the entire surface shows highly brittle cleavage facets with the large size of each facet caused by the ferrite grain size. The surface of the Group 4 sample shows a slight depth of ductility in the initiation region, transitioning to quasi-cleavage for the remainder of the surface. The initiation area below the notch in the Group 5 sample appears to be ductile, with only microvoid coalescence, which transitions to a combination of quasi-cleavage and microvoid coalescence in the center region, returning to microvoid coalescence in the final fracture area.
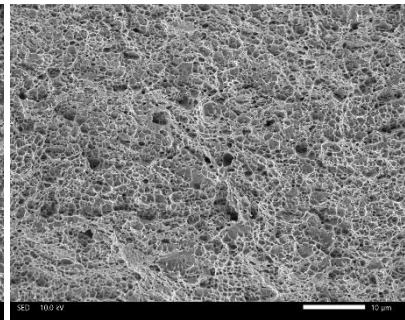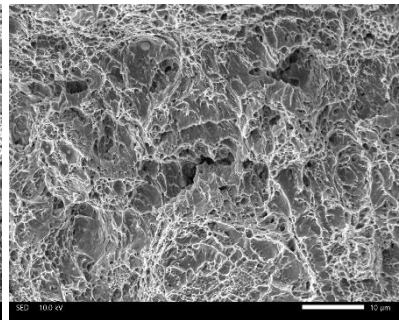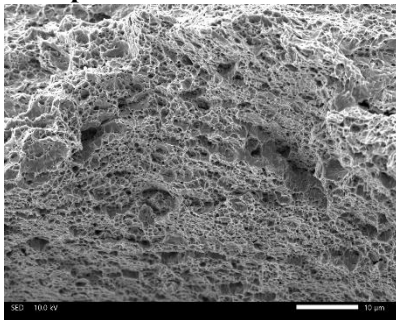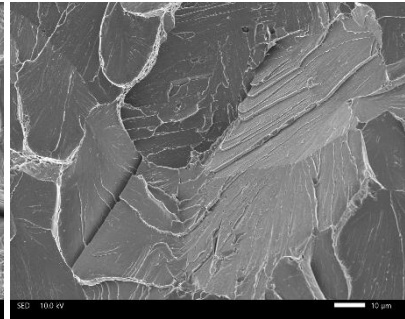
Fracture Initiation   **Unstable Fracture**   **Final Fracture**

Group 1 – 46.2 J
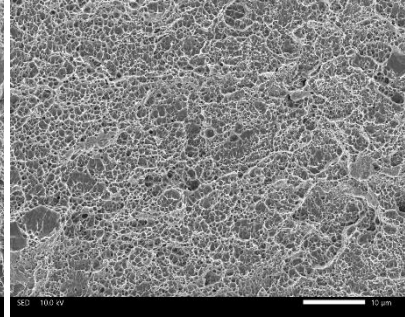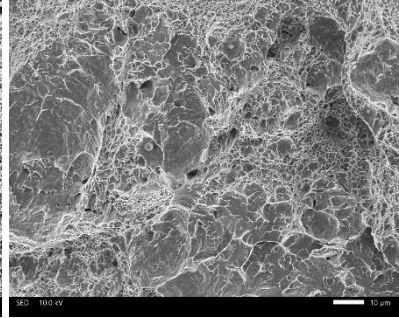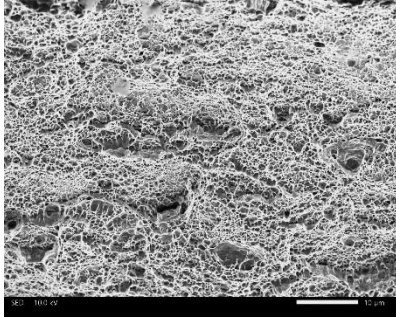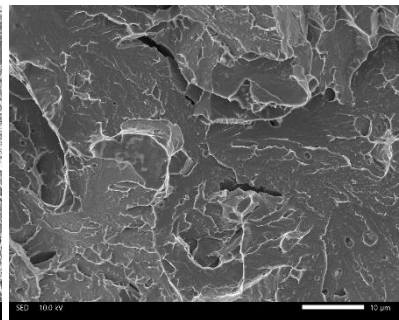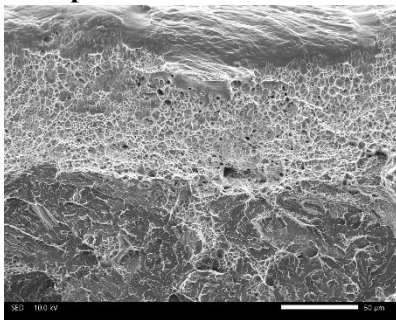

Group 2 – 179.7 J

Group 3 – 6.8 J
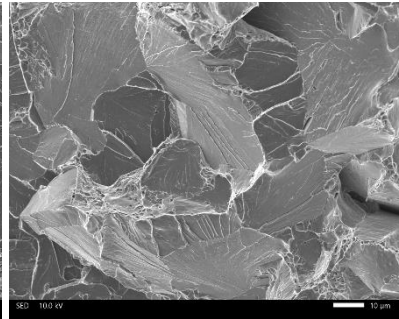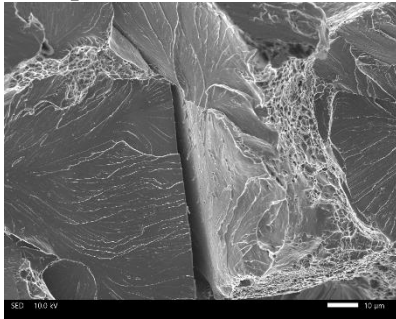
Group 4 – 24.7 J
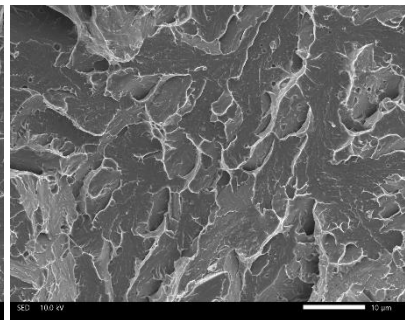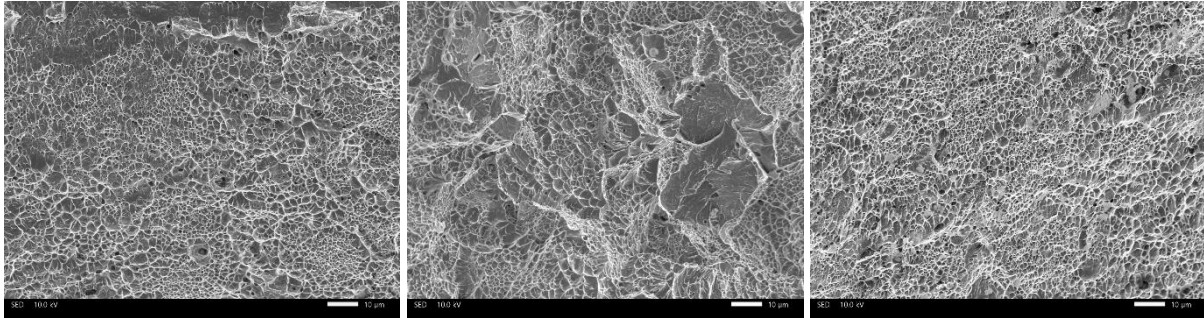
Group 5 – 54.6 J

Figure 15. SEM/SEI of the fracture surfaces from representative bars in each group. All photos are oriented with the progression of fracture moving from the top of the frame to the bottom. In the left column, the initial fracture region, the bottom edge of the notch is located at or slightly above the top of the image. Characteristics of the fracture vary by group and in some cases, location on the surface. Although several magnifications were used to include specific features, the scale markers are 10 μm for all images except the initial fracture area in Group 4, which is 50 μm to show the location of the microvoid coalescence to quasi-cleavage transition.

The five sample groups are divided into two basic microstructure-related categories, those with ferrite as the primary transformation product and those that are mostly bainitic. The fracture surfaces from the bainitic samples, groups 1, 4, and 5 all display a combination of microvoid coalescence and quasi-cleavage to varying degrees. Exmining the fracture surfaces in Figure 15, it appears that the impact energy decreases as the amount of quasi-cleavage increases. Furthermore, reviewing Figures 6, 11, and 12, the etched microstructure images from the bainitic category, it appears the uniformity of the bainitic microstructure could be an indicator of a reduction in the impact energy. Roughly speaking, it appears group 5 has the most uniform bainitic microstructure, followed by group 1, with group 5 showing the most separation of the bainite carbides and precipitate-free ferrite. This order of increasing uniformity in bainite transformation is the same as the trend from lowest impact energy to highest in the bainitic category.

The remaining samples from groups 2 and 3 are the primarily ferritic samples and the extremes in impact energy in this study. The microstructures from the thermal processing produced distinctly different microstructures, although both were still predominantly ferritic. Where the microstructure from group 2 contained small grain ferrite with nanometer size carbides precipitated throughout the microstructure, the group 3 microstructure showed a comparatively large grain growth and a change in the location of the carbide precipitates to include a large number precipitating and covering the grain boundaries. These grain boundary precipitates can embrittle the microstructure and contribute to a more brittle fracture, which is present in Figure 15.

CONCLUSIONS

Similar to what was shown in the previous papers, it was observed that this FSLA Mod steel can be heat-treated to create a variety of microstructures and resulting strengths (energies). A few of the conclusions from the study are listed below:

- Intercritical annealing controls the amount and type of transformation products by concentrating the alloying elements into the different high temperature phases. Upon cooling, ferrite is unchanged because it is stable at room temperature and the austenite transforms to a higher hardness product.
- Elemental partitioning modifies the mixture of transformation products and affects the hardness and strength of ferrite by concentrating a portion of the alloying elements into the high temperature austenite, thus increasing the local hardenability.
- When heating in a temperature range where ferrite is the primary phase, carbides have been shown to precipitate as nanometer-size features in both grain interiors and grain boundaries. These may be the initiation sites for the creation of microvoids.
- If a dual phase microstructure is present at the austenitizing temperature, carbides precipitate only in the ferrite since carbon is soluble in austenite.
- In the absence of strong carbide forming elements like V and Nb, the carbide precipitates contain a large amount of Mo.
- Austenitizing, then reducing and holding the temperature into the primarily ferrite phase field was shown to cause grain growth and carbide precipitation into grain boundaries. These grain boundary precipitates may be long and thin or possibly as sheets that decorate and embrittle the boundaries.
- The impact strength of the primarily bainitic samples roughly correlates to the amount of precipitate-free ferrite.
- Samples containing the most microvoid coalescence also appeared to have the highest impact energy.

REFERENCES

1. C. Schade, T. Murphy, K. Horvay, A. Lawley, and R. Doherty, "Development of a Free Sintering Low Alloy (FSLA) Steel for the Binder Jet Process", *Advances in Additive Manufacturing with Powder Metallurgy – 2021*, compiled by S. Atre and S. Jackson, Metal Powder Industries Federation, Princeton, NJ, 2021, part 7, pp. 287-306.
2. C. Schade, T. Murphy, and K. Horvay, "Microstructure and Mechanical Properties of FSLA Steel Produced by the Binder Jet Process", *Advances in Additive Manufacturing with Powder Metallurgy – 2022*, compiled by A. Bose and J. Sears, Metal Powder Industries Federation, Princeton, NJ, 2022, part 6, pp. 343-355.
3. L. Donoho, D. Webster, T. Murphy, and C. Schade, "Microstructure and Mechanical Properties of FSLA Steel Produced by the Metal Injection Molding", *Advances in Powder Metallurgy and Particulate Materials – 2022*, compiled by P. Hauck and T. McCabe, Metal Powder Industries Federation, Princeton, NJ, 2022, part 4, pp. 169-179.
4. C. Schade, T. Murphy, and K. Horvay, "Development of a Dual Phase - Low Alloy Steel for Laser Powder Bed Fusion (LPBF)", *Advances in Additive Manufacturing with Powder Metallurgy – 2023*, Compiled by S. Joens and M.K. Johnston, Metal Powder Industries Federation, Princeton, NJ, 2023, part 7, pp. 472-488.
5. T. Murphy, C. Schade, & K. Horvay, "Microstructure and Mechanical Properties of Free-Sintering Low-Alloy Steel Produced by Three Additive Manufacturing Methods", *International Journal of Powder Metallurgy*, 2023, vol. 59, no. 4, pp. 31-45.
6. R.M. German, *Sintering Theory and Practice*, First Edition, 1996, John Wiley & Son, New York, NY.

7. T.M. Puscas, A. Molinari, J. Kazior, T. Pieczonka, and M. Nykiel, "Sintering Transformations in Mixtures of Austenitic and Ferritic Stainless Steel Powders", *Powder Metallurgy*, 2001, Vol. 44, No. 1, pp. 48-52.

8. R.I. Sands and J.F. Watkinson, "Sintered Stainless Steels I.- The Influence of Alloy Composition Upon Compacting and Sintering Behaviour", *Powder Metallurgy*, 1960, Vol. 3, No. 5, pp. 85-104.

9. N.B. Shaw and R.W.K. Honeycombe, "Some Factors Influencing the Sintering Behaviour of Austenitic Stainless Steels", *Powder Metallurgy*, 1977; Vol. 20, No. 4, pp. 191-198.

10. ArcelorMittal, Dual phase steels, Chemical composition, Cold rolled steel, https://automotive.arcelormittal.com/products/flat/first_gen_AHSS/DP

11. ASTM Standard Test Method E23, "Standard Test Methods for Notched Bar Impact Testing of Metallic Materials", *Book of ASTM Standards*, Vol. 03.01, 2023, ASTM International, West Conshohocken, PA.

12. ASTM Standard Test Method E23, "Standard Test Methods for Notched Bar Impact Testing of Metallic Materials", *Book of ASTM Standards*, Vol. 03.01, 2001, ASTM International, West Conshohocken, PA.

13. Charpy Impact Steel Testing: Part One, Figure 2, https://www.totalmateria.com/en-us/articles/charpy-impact-steel-testing-1.

14. The Hand Book on Mechanical Maintenance – Impact Test, Compiled by K.P. Shah, https://practicalmaintenance.net/?p=968,

15. ASTM Standard Test Method E562, "Determining Volume Fraction by Systematic Manual Point Count", *Book of ASTM Standards*, Vol. 03.01, 2023, ASTM International, West Conshohocken, PA.

16. ASTM Standard Test Method E112, "Standard Test Methods for Average Grain Size", *Book of ASTM Standards*, Vol. 03.01, 2023, ASTM International, West Conshohocken, PA.

17. ASTM Standard Test Method E384, "Standard Test Method for Microindentation Hardness of Materials", *Book of ASTM Standards*, Vol. 03.01, 2023, ASTM International, West Conshohocken, PA.